Agricultural and Forest Meteorology 350 (2024) 109996

Contents lists available at ScienceDirect

Agricultural and Forest Meteorology

journal homepage: www.elsevier.com/locate/agrformet

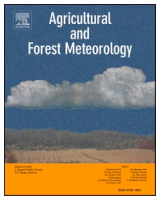

Surface-atmosphere energy exchanges and their effects on surface climate and atmospheric boundary layer characteristics in the forest-tundra ecotone in northwestern Canada

Vincent Graveline [a,b,*], Manuel Helbig [b], Gabriel Hould Gosselin [a], Haley Alcock [a], Matteo Detto [c], Branden Walker [d], Philip Marsh [d], Oliver Sonnentag [a]

[a] Département de Géographie & Centre d'Études Nordiques, Université de Montréal, Montréal, Québec, Canada
[b] Department of Physics & Atmospheric Science, Dalhousie University, Halifax, Nova Scotia, Canada
[c] Department of Ecology and Evolutionary Biology, Princeton University, Princeton, New Jersey, USA
[d] Department of Geography and Environmental Studies, Wilfrid Laurier University, Waterloo, Ontario, Canada

ARTICLE INFO

Keywords:
Surface energy balance
Atmospheric boundary layer
Surface properties
Forest-tundra ecotone
Eddy covariance
Mixed-layer slab model

ABSTRACT

The circumpolar forest-tundra ecotone is experiencing rapid changes in vegetation composition and structure. Collectively, these changes modify surface-atmosphere energy exchanges and thus characteristics of the atmospheric boundary layer (ABL). Here, we characterize differences in bulk surface properties and resulting energy balance components using multi-year eddy covariance and supporting measurements made at a mineral upland tundra and a nearby subarctic woodland site between 2013 and 2022. The two sites are characteristic of the forest-tundra ecotone of northwestern Canada. A mixed-layer slab model, in combination with radiosonde observations, was used to gain more insights into differences in ABL characteristics. Compared to the tundra, the tree cover of the woodland led to an enhanced ability to transfer heat into the atmosphere, a higher resistance to evapotranspiration and a stronger coupling between surface and atmosphere. Sensible heat flux (H) was generally higher at the woodland than at the tundra. The largest difference in daily mean H was observed in late winter and spring when the albedo of the snow-covered landscape at the woodland was reduced by 45% compared to the tundra. Both sites experienced similar latent heat flux throughout the year. At the woodland, modelled afternoon air temperature in the mixed layer was up to 9 °C higher in spring and up to 3 °C higher in summer compared to the tundra. In accordance with model results, radiosonde observations indicated a deeper ABL and higher air temperature at the woodland. The presence of trees in the southern part of the forest-tundra ecotone increases air temperature throughout the year and has a drying effect in spring. Consequently, vegetation shifts in the forest-tundra ecotone can be expected to modify local surface climate change patterns, which must be considered when assessing climate change impacts in the region.

1. Introduction

The Arctic-boreal region plays an important role in the global climate system through its exchange of energy, matter, and momentum with the atmosphere (McGuire et al., 2006). Air temperature across the Arctic-boreal region has been increasing at disproportionately high rates compared to the global average (Rantanen et al., 2022). Together with climate warming, altered precipitation patterns (Trenberth, 2011), increased atmospheric carbon dioxide (CO_2) concentration (Zhu et al., 2017), and intensifying disturbance regimes (Foster et al., 2022) have led to changes in vegetation composition and structure across the Arctic-boreal region (Myers-Smith et al., 2011; Wang et al., 2020). The Arctic-boreal region includes the forest-tundra ecotone (FTE), separating the boreal biome to the south from the Arctic biome to the north

Abbreviations: ABL, Atmospheric boundary layer; FTE, Forest-tundra ecotone; HPC, Havikpak Creek; TVC, Trail Valley Creek; MAAT, Mean annual air temperature; MATP, Mean annual total precipitation; MSAT, Mean summer air temperature; MSTP, Mean summer total precipitation; MWAT, Mean winter air temperature; MWTP, Mean winter total precipitation; Ω, Decoupling factor; β, Bowen ratio; zi, Atmospheric boundary layer height; σ, Albedo; $\Delta\theta$, diurnal changes in mixed-layer potential temperature; Δq, diurnal changes in mixed-layer specific humidity; CLASS, Chemistry Land-surface Atmosphere Soil Slab model.

* Corresponding author at: 1375, ave Thérèse-Lavoie-Roux, Montréal, QC, H2V 0B3, 1375, ave Thérèse-Lavoie-Roux, Montréal, QC, H2V 0B3.
E-mail addresses: vincent.graveline@umontreal.ca (V. Graveline), oliver.sonnentag@umontreal.ca (O. Sonnentag).

https://doi.org/10.1016/j.agrformet.2024.109996
Received 28 November 2023; Received in revised form 7 March 2024; Accepted 29 March 2024
Available online 6 April 2024

over a width of only a few hundred kilometers (Timoney et al., 1992; Montesano et al., 2020). Vegetation and thus ecosystem composition and structure vary considerably across the FTE as trees become, from south to north, shorter and stunted, sparser, and eventually, absent. The associated steep latitudinal gradient in surface properties (e.g., albedo) results in corresponding latitudinal variations in how the FTE exchanges energy and matter with the atmosphere. For example, albedo increases with the parsity of tree cover, where relatively "dark" black spruce (*Picea mariana*) dominated forests transition into relatively "bright" Arctic tundra ecosystems (Beringer et al., 2005). Changes in vegetation structure and composition across the FTE could modify surface-atmosphere energy exchanges and, thus, dynamics of the atmospheric boundary layer (ABL; e.g., height, temperature, and humidity). To better understand the impacts of potential vegetation distribution and composition changes on surface climate and ABL dynamics across the FTE, a comprehensive characterization of surface-atmosphere interactions is needed.

In situ and remote sensing observations, and projections with global dynamic vegetation models have suggested a northward shift of the FTE in some parts of the circumpolar Arctic-boreal region (Berner and Goetz, 2022; Gonzalez et al., 2010; Harsch et al., 2009; Pearson et al., 2013; Scheffer et al., 2012; Zhang et al., 2013). This shift is commonly manifested by densification and/or the northward encroachment by trees and/or taller shrubs (Tape et al., 2006). For example, studies using satellite remote sensing data products reported positive trends in spectral indices (i.e., interpreted as 'Arctic greening') attributed to an increase in aboveground biomass and/or productivity (Goetz et al., 2005). However, other studies reported negative trends in spectral indices (i.e., interpreted as 'Arctic browning') (Phoenix and Bjerke, 2016). These opposite trends highlight the complexity in interpreting remote sensing observations and projecting vegetation redistributions across the Arctic-boreal region in a circumpolar context. Changing arctic sea ice conditions suggest that the advancement of forest-tundra ecotones in western Siberia is imminent, whereas those in northern Canada will likely remain stagnant for longer (Dial et al., 2024). While the advancement of the FTE is still debated (Timoney and Mamet, 2020), in the Inuvialuit Settlement Region in northwestern Canada, one among the most rapidly warming regions of the Earth (Chylek et al., 2022; Rantanen et al., 2022), the presence of taller and more productive shrubs, but not trees, has been documented (Lantz et al., 2012).

Observations of the exchange of energy and matter between ecosystems and the atmosphere (at the scale of hundreds of square meters) can be carried out with micrometeorological techniques including eddy covariance (Baldocchi et al., 1988). However, only a few studies have examined surface-atmosphere exchanges within the FTE with eddy covariance (e.g., Beringer et al., 2005) or other micrometeorological techniques (Lafleur and Rouse, 1995). For example, Lafleur and Rouse (1995) compared turbulent fluxes of latent heat (LE) and sensible heat (H) between a boreal forest stand and a wetland tundra in the FTE of the Hudson Bay Lowlands in Manitoba, Canada during the summers (June to August) of 1989 to 1993 using the Bowen ratio technique. There, H and LE were larger and smaller, respectively, over the boreal forest stand than over the tundra wetland. Similar findings were reported from five sites in the FTE of the Seward Peninsula in western Alaska, US (Beringer et al., 2005). Differences in diurnal heat (i.e., H) and moisture input (i.e., LE) in the atmospheric boundary layer (ABL) can lead to different ABL growth dynamics affecting its effective heat capacity (i.e., how much energy is needed to change the temperature of the ABL, which is related

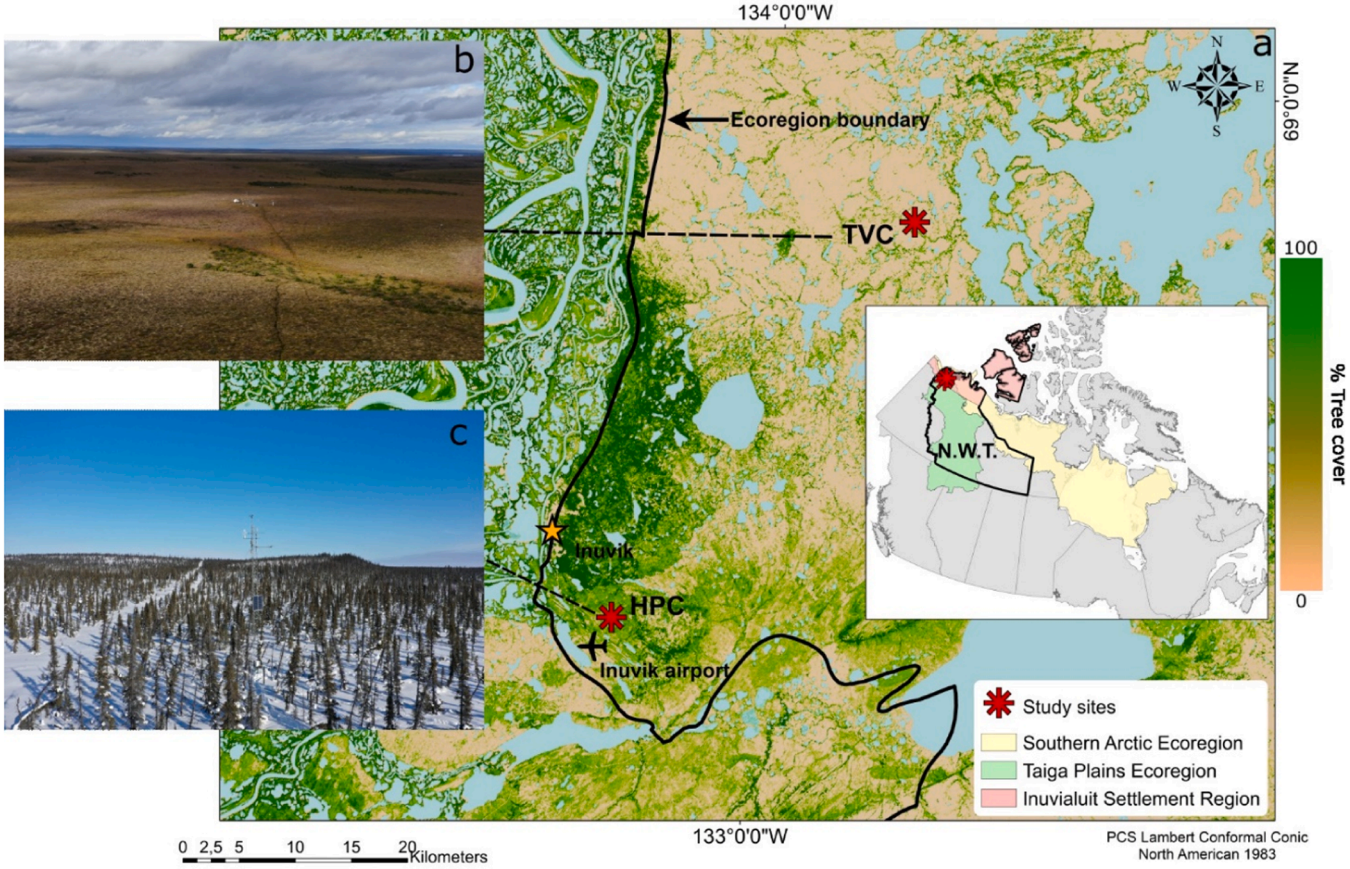

Fig. 1. a) Location of the two study sites characteristic of the forest-tundra ecotone between the Taiga Plains and Southern Arctic ecozones of northwestern Canada: b) Trail Valley Creek (TVC, mineral upland tundra) and c) Havikpak Creek (HPC, subarctic woodland). The backdrop map is the Global 2010 Tree Cover product (Hansen et al., 2013). Images source: Branden Walker.

to the volume of air through which the heat is mixed), and the rate of dry-air entrainment from the free atmosphere (Baldocchi et al., 2000; Davy and Esau, 2016; Helbig et al., 2021; Vila-Guerau de Arellano et al., 2015).

Here, we synthesised multi-year eddy covariance and supporting measurements from two nearby eddy covariance tower sites (ca. 50 km apart) representing the FTE in the Inuvialuit Settlement Region (Fig. 1): a subarctic woodland ('woodland') and a mineral upland tundra ('tundra') near Inuvik, NWT. The goal of this study was to develop a baseline understanding of the latitudinal variation in surface-atmosphere energy exchanges and surface climate characteristics across the FTE in northwestern Canada. To meet this goal, our three objectives were to 1) quantify seasonal differences in daily woodland and tundra energy exchanges, 2) examine bulk surface parameters to explain drivers of energy exchange differences between woodland and tundra, and 3) quantify the effects of woodland and tundra energy partitioning on ABL dynamics and characteristics with a mixed-layer slab model and radiosonde observations. Characterization of baseline surface-atmosphere interactions is needed to develop a predictive understanding of tree or shrub densification and/or encroachment on surface climate in the circumpolar Arctic-boreal region.

2. Methods

2.1. Study sites

Paired eddy covariance and supporting measurements were made at two long-term research sites during 2013–2022: Havikpak Creek (HPC; 68° 19′ 13.3″ N 133° 31′ 7.4″ W, ~80 m a.s.l.), ca. 10 km south of Inuvik, NWT in the northern part of the Taiga Plains ecozone, and Trail Valley Creek (TVC; 68° 44′ 31.29″ N, 133° 29′ 56.87″ W, ~85 m a.s.l.) ca. 45 km north of Inuvik, NWT in the southern part of the Southern Arctic ecozone (Fig. 1). Havikpak Creek is a subarctic woodland on undulating, hummocky terrain mostly formed by moderately well-drained glacial till and overlain by silty clay and a thin organic layer (Eaton et al., 2001). The vegetation at HPC comprises scattered, stunted, mostly mature (>70 years old) black spruce (*Picea mariana*) trees with a mean canopy height of 2.4 m (Qu et al., 2023). Havipak Creek is predominantly covered by forest (>50%) followed by alder shrubs, short grass, moss, and lichen. Leaf area index (LAI) was optically measured using a Plant Canopy Analyzer (LAI-2200, LI-COR Biosciences Inc., Lincoln, NE) following methods described elsewhere (Ryu et al., 2010; Sonnentag et al., 2007a, b). The mean LAI (± one standard deviation) for overstory (i.e., tree) and understory (i.e., shrub) was 0.34 (± 0.16, $n = 40$) and 0.51 (± 0.19, $n = 40$), respectively.

Trail Valley Creek is a mineral upland tundra on slightly undulating, hummocky terrain of similar glacial origin as HPC, and incised by several narrow river and creek valleys. The low-stature tundra vegetation (<0.3 m in height, LAI = 0.35 [± 0.24, $n = 54$]) at TVC comprises dwarf shrubs (e.g., birch [*Betula nana, Betula glandulosa*], alder [*Alnus* sp.], willows), grasses and tussocks (cotton grass [*Eriophorum* spp.]), and patches of lichen and mosses. In addition, the surrounding lake-rich landscape at TVC also includes several periglacial tundra landforms and associated cover types including ice-wedge polygons and barren ground. Both HPC and TVC are underlain by continuous permafrost (i.e., >90% in areal extent; Gruber, 2012), with active layers ranging from 40 to 80 cm at HPC (Qu et al., 2023) and > 80 cm at TVC (Eaton et al., 2001). Detailed site descriptions for HPC and TVC can be found elsewhere (e.g., Eaton et al., 2001; Krogh and Pomeroy, 2018; Marsh and Pomeroy, 1996; Wallace and Baltzer, 2019; Wilcox et al., 2019).

The climate of the region is subarctic with short, warm to cool summers (June to September) and long, cold winters (October to May) (Beck et al., 2018). For the period 1991–2020 (climate normal), mean annual air temperature (MAAT) was −7.8 ± 0.7 °C and mean annual total precipitation (MATP) was 245 ± 11 mm at HPC. For comparison, TVC is generally colder and drier than HPC with MAAT of −8.4 ± 0.7 °C and MATP of 210 ± 9.1 mm for the same period (Hopkinson et al., 2011; McKenney et al., 2011; Xu and Hutchinson, 2013). About two thirds of MATP falls as snow. Over the study period (2013–2022), both HPC and TVC experienced similar variations in mean monthly air temperature and mean monthly total precipitation (Fig. S1). None of the study years was characterized by extreme air temperature or precipitation anomalies (defined as years with air temperature or precipitation anomalies exceeded more than two standard deviations from the climate normals, 1991–2020). The landscapes containing TVC and HPC have both become significantly warmer since 1980 based on the Wilcoxon rank-sum test ($\alpha = 0.05$) (Fig. S2). Since 1980, mean annual air temperature has increased by 0.6 ± 0.3 °C per decade while winter (mid-October to mid-March) air temperature has increased more rapidly at 0.8 ± 0.2 °C per decade for both sites.

2.2. Eddy covariance and supporting measurements

Turbulent momentum and energy fluxes were measured using the eddy covariance technique (Baldocchi et al., 1988). The eddy covariance systems at TVC and HPC comprised identical three-dimensional sonic anemometers (CSAT3A; Campbell Scientific Inc., Logan, UT) and open-path infra-red gas analyzers (EC150; Campbell Scientific Inc.) to measure high-frequency fluctuations (10 Hz) in vertical wind velocity, and carbon dioxide and water vapour densities. Mounted on horizontal booms on tower structures at 11.8 m (HPC) and 4.2 m (TVC) above the mean ground surface, the measurement heights provided sufficient fetch (several hundred meters) in all directions. Thus, flux footprints covered representative subarctic woodland (HPC) and mineral upland tundra source areas (TVC). Micrometeorological and eddy covariance instruments were controlled and logged using CR3000 data loggers (Campbell Scientific Inc.). The eddy covariance systems were generally serviced twice a year, before snowmelt in late winter (April) and in late summer (August). Servicing consisted in performing routine maintenance according to Campbell Scientific recommendations, and water vapour zero and span calibration using gas standards and a dew point generator (LI-610; LI-COR Biosciences Inc., Lincoln, NE). The TVC time series has a data gap from November 2014 to August 2015 due to instrument failure. The TVC and HPC tower structures were deemed unsafe to climb in early 2014. Replacement tower structures were erected in 2015 at HPC and 2016 at TVC. Both towers were reinstrumented in August 2016, replicating the original instrumental set-up (i.e., height, orientation). Consequently, the HPC time series has a data gap from December 2013 to August 2016.

Half-hourly turbulent fluxes of latent heat (LE, W m^{-2}) and sensible heat (H, W m^{-2}) were calculated using the EddyPro software package (version 7.0.6; LI-COR Biosciences Inc). At both sites, a double-rotation method was applied to rotate the coordinate system of the sonic anemometer into the mean streamlines of the wind field (Wilczak et al., 2001). We removed spikes in the high-frequency time series (Vickers and Mahrt, 1997), corrected fluxes for spectral attenuation (Moncrieff et al., 1997), and accounted for air density fluctuations (Webb et al., 1980; Detto and Katul, 2007) and humidity effects (Van Dijk et al., 2004). Storage fluxes were calculated using the one-point method, which consists in calculating temporal changes of the air temperature and specific humidity measured at the eddy covariance system measurement height and assuming a constant temperature and humidity profile in the air column underneath.

In post-processing, we applied a three-class quality flag system to retain only high-quality data for analysis (i.e., quality flags 0 and 1; Mauder and Foken, 2011). Any remaining outliers in the half-hour time series were filtered using a spike-detection algorithm (Papale et al., 2006) and fluxes during periods with friction velocity below 0.1 m s^{-1} were removed. Turbulent fluxes were gap-filled using the Marginal Distribution Sampling algorithm described in Reichstein et al. (2005). Remaining long winter gaps were filled with mean half-hour averages for the same days and hours in the remaining years. Further details on

the data processing are provided in Helbig et al. (2016) and (2017). All analyses were done on daily LE and H for "good" days defined as days for which less than 24 half hours were missing (i.e., <50%).

Net radiation (R_n, W m^{-2}) at HPC and TVC was measured using four-component net radiometers (HPC: CNR1, TVC: CNR1 2013 to August 2019 and CNR4 August 2019 onwards; Kipp and Zonen, Delft, the Netherlands) installed on south-facing booms at 11.8 m and 4.2 m above the mean ground surface, respectively. Ground heat flux (G, W m-2) at both sites was measured with heat flux plates at a depth of 10 cm at HPC and 8 cm at TVC (HFT3 [Hukseflux, Delft, the Netherlands]). Soil temperature and volumetric water content above the heat flux plates were measured with TCAV temperature averaging thermocouple arrays and CS616 soil moisture probe (both Campbell Scientific Inc.), where TCAV probes were evenly spread vertically from the heat flux plate to 1 cm below the surface and CS616 at the mid point. Organic layer thickness at TVC varies with prevailing vegetation around the EC tower, ranging from approximately 1 cm to 2 cm in lichen patches to over 30 cm in areas dominated by shrubs and tussocks. Consequently, both Organic and inorganic near surface soils were instrumented with heat flux systems. At HPC, the top portion of the active layer is entirely organic soil, heat flux systems were installed in a hummock and a hollow to capture microtopography driven heterogeneity in G. Volumetric water content measurements were corrected according to soil type using the method of Rowlandson et al. (2013). Heat storage change above the heat flux plate was calculated for every half hour using volumetric heat capacity of soil, air, and water according to the method described in Wisser et al. (2011). Ground heat flux at the surface was subsequently calculated by adding the measured flux at the plate depth, to the energy stored in the layer above as described in the HFT3 user manual. Air temperature (T_{air}, °C) and relative humidity (RH,%) were measured at 13.8 m (HPC) and 4.6 m (TVC) using temperature-humidity probes (HC2S3; Campbell Scientific Inc.). Tower-based potential temperature and specific humidity were calculated with T_{air}, air pressure and RH.

Energy balance closure was calculated as the regression slope of the daily sum of half-hourly turbulent fluxes [$H + LE$] and available energy [Rn–G] during the summer (June-July-August). Winter and shoulder seasons, spring and fall, were excluded to minimize uncertainties introduced by additional energy balance terms (e.g., snow melt, melt energy from ground ice). Energy balance closure was 0.95 and 0.73 at TVC and HPC, respectively, falling within previously reported ranges (Stoy et al., 2013; Wilson et al., 2002). No corrections were done on energy balance closures.

2.3. Mixed-layer slab model

To quantify the effects of woodland (HPC) and tundra (TVC) surface fluxes on ABL dynamics, we used a mixed-layer slab model (Chemistry Land-surface Atmosphere Soil Slab model [CLASS]; Vila-Guerau de Arellano et al., 2015). The CLASS model is based on the assumption that potential temperature (θ, K) and specific humidity (q, g kg^{-1}), and wind components in the mixed layer are constant with respect to height. In the absence of advective fluxes, changes of θ and q within the mixed layer result from the combined effects of surface and entrainment fluxes of H and LE (Stull, 1988). We used CLASS to simulate diurnal and seasonal changes in ABL dynamics as characterized by daily afternoon estimates of ABL height (z_i, m), defined as the base of the underlying temperature inversion, and mixed-layer θ and q obtained with CLASS, and the contribution of surface and entrainment fluxes to changes in mixed-layer θ and q. In CLASS, the entrainment velocity determines the input of heat and humidity from the free atmosphere into the mixed layer, and the growth of the mixed layer. The entrainment velocity in CLASS is calculated based on the assumption that the entrainment fluxes of virtual potential temperature is a constant fraction of the surface heat fluxes, here assumed as 0.2. The model was forced with half-hourly gap-filled H and LE from 05:00 MST and 17:00 MST, corresponding to early morning and late afternoon launch times of operational radiosondes from the Inuvik Upper Air Weather Station (ca. 700 m south-east of HPC). Days with consistent negative H were discarded since they do not meet requirements for mixed-layer growth. A detailed description of CLASS is given elsewhere (Tennekes, 1973; Tennekes and Driedonks, 1981; van Heerwaarden and Teuling, 2014; Vila-Guerau de Arellano et al., 2015).

The CLASS model requires initial estimates of jumps in θ (K) and q (kg^{-1}) at z_i, lapse rates of potential temperature (K m^{-1}) and specific humidity (kg^{-1} m^{-1}) in the free atmosphere, and initial θ and q in the mixed layer. Given the proximity of the two sites, initial estimates of θ and q jumps at z_i were set the same at TVC and HPC and defined as the difference between θ and q at z_i and their means within the mixed layer as derived from afternoon radiosonde observations from the Inuvik Upper Air Weather Station. Lapse rates in the free atmosphere were estimated as the slope parameter of linear regressions of height on θ and q (from 05:00 MST radiosonde profiles) using measurements from all levels between 1000 m and 6000 m above ground as in Helbig et al. (2020) and were kept constant throughout the day. Initial θ and q in the mixed layer were set using tower measurements at 05:00 MST. The effect of large-scale subsidence velocity on ABL growth was evaluated and calculated using hourly horizontal divergence (s^{-1}) from ERA5 reanalysis (Hersbach et al., 2023) at 750 hPa (~ 2500 m above the ground; around the maximum z_i) but was found to be negligible. The effect of wind shear at the surface was not considered in the calculation of the entrainment velocity. The model was run for cloudy and clear-sky days. Cloudy days were defined as days with less than 70% of daily potential solar radiation expected for the latitude. Daily potential solar radiation for the latitude was calculated in the R computing environment (v4.0.3; R Core Team, 2020) using the "potential.radiation" function from the R package 'bigleaf' (v0.8.2, Knauer et al., 2018).

2.4. Radiosonde observations

Daily estimates of z_i, and mixed-layer θ and q at HPC obtained with CLASS were evaluated against radiosonde observations made at the Inuvik Upper Air Weather Station near HPC (operational radiosonde data available from the University of Wyoming's Department of Atmospheric Science repository at http://weather.uwyo.edu/upperair/sounding.html). Radiosonde data were filtered to keep only soundings showing a well-defined mixed layer and unstable or neutral atmospheric conditions. Thus, soundings with constantly increasing θ with altitude were discarded, indicating stable atmospheric conditions. To ensure the presence of a well-mixed layer and minimize the effect of horizontal advection, radiosonde θ profiles with a standard deviation higher than 1 K in the mixed layer were also discarded. Only days with both available morning and afternoon soundings and matching days with high-quality surface flux observations (i.e., less than 50% of gaps) were used. The ABL height was derived for afternoon radiosonde profiles using the 'parcel' method with an excess temperature of 1 K added to the first measurement height near the surface (Holzworth, 1964; Seibert, 2000). An excess temperature was applied to ensure the representation of a superadiabatic layer near the ground that was often missing, especially when the first measurement in the radiosonde profile was well above the ground. The lowest measurement was often at ground surface but extended to 20 to 200 m above ground surface in some cases. The ABL height was defined as the first height measurement at which radiosonde θ is equal to or higher than radiosonde θ at the surface (Fig. S3) (Seidel et al., 2010).

Additionally, radiosonde observations from two summer campaigns at TVC in early June 2021 and late August 2022 were used for comparison with corresponding estimates obtained with CLASS at TVC (Fig. S3). High-resolution (1 m) reusable radiosondes (S1H2, Sparv Embedded AB, Linkoping, Sweden; Bessardon et al., 2019) were launched with twelve launches at around 17:00 MST when clear-sky conditions were present (Fig. S4). Out of 40 radiosonde launches, three matched with days of high-quality surface flux observations

suitable for forcing CLASS. Radiosondes were generally dropped between 1 and 2 km above the ground surface to allow their recovery on foot. No measurements were made from the descending sondes. Radiosonde observations at TVC were also compared to radiosonde observations at HPC made at the Inuvik Upper Air Weather Station.

2.5. Analysis

We defined distinct seasons (winter, spring, summer, fall) based on pooled R_n measurements made at HPC and TVC. Using daily mean R_n across years (2013–2022), the start of winter was defined when $R_n < 0$ W m^{-2}, start of spring and fall when $R_n > 0$ W m^{-2} and start of summer when $R_n >= 100$ W m^{-2} for three or more consecutive days (Oechel et al., 2014). In addition, winter was further subdivided into 'early winter' (i.e., from the start of winter to the end of the year) and 'late winter' (i.e., from the start of the year to the end of winter). The mean (2013–2022) of the site-specific day-of-year (DOY) of the start of each season at HPC and TVC was used as the season definition for the FTE in the Inuvialuit Settlement Region (Fig. 2).

To shed light on daily, and seasonal differences (spring, summer, fall) in woodland (HPC) and tundra (TVC) surface energy exchanges, we examined five widely used bulk surface parameters (Baldocchi and Ma, 2013; Beringer et al., 2005; Helbig et al., 2016; Helbig et al., 2020; Ryu et al., 2008): albedo (α, unitless; Ahmad and Lockwood, 1979), aerodynamic conductance (G_a, m s^{-1}; Thom, 1972), surface conductance of water vapour (G_s, m s^{-1}; Monteith., 1965), decoupling factor (Ω, unitless; Jarvis and McNaughton, 1986) and Bowen ratio (β, unitless; Lewis, 1995). Using high-quality half-hourly fluxes of H and LE from 12 MST to 16 MST (i.e., two hours before to two hours after solar noon), the six bulk surface parameters were calculated using the R package 'bigleaf' (v0.8.2, Knauer et al., 2018). After discarding outliers in half-hourly bulk surface parameter estimates based on visual inspection, median daily bulk surface parameters were calculated. Median daily spring, summer and fall bulk surface parameters for HPC and TVC were tested for significant differences based on the Wilcoxon rank-sum test ($\alpha = 0.05$).

The performance of CLASS to reproduce ABL dynamics at HPC was assessed, first, qualitatively by comparing modelled mean (2013–2022) afternoon z_i and modelled diurnal changes in mixed-layer θ ($\Delta\theta$, °C) and q (Δq, g kg^{-1}), calculated as the difference between modelled θ and q at 17:00 MST and initial θ and q at 05:00 MST, respectively, to corresponding estimates of z_i, $\Delta\theta$, Δq from the radiosonde observations at HPC. Every day, radiosonde estimates of $\Delta\theta$ and Δq were calculated as the difference between afternoon (17:00 MST) profile mean θ and q and the near-surface θ and q from the morning profiles (05:00 MST), respectively. Daily contributions of surface and entrainment H and LE to modelled $\Delta\theta$, Δq were estimated as the cumulative sum of half-hourly observed surface kinematic fluxes, and modelled entrainment kinematic H and LE, at HPC and TVC. Second, we used orthogonal linear regression and associated metrics (coefficient of determination [R^2], mean average error [MAE]) to assess the CLASS model's ability to reproduce daily radiosonde estimates of z_i, $\Delta\theta$, and Δq between 2013

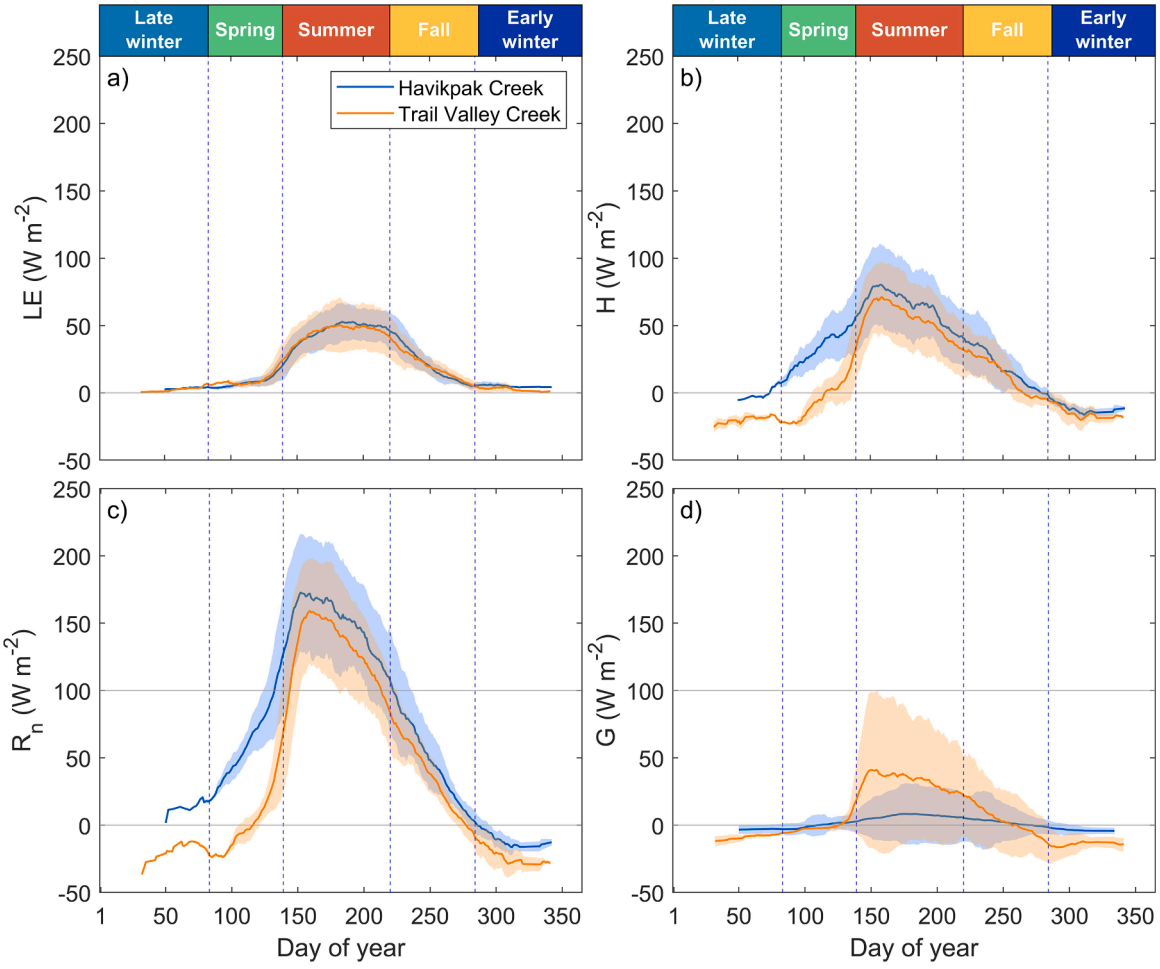

Fig. 2. Fourteen-day moving averages of energy balance components across all years (2013–2022): a) latent heat flux (LE, W m^{-2}), b) sensible heat flux (H, W m^{-2}), c) net radiation (R_n, W m^{-2}) and d) ground heat flux (G, W m^{-2}) at Havikpak Creek (woodland) and Trail Valley Creek (tundra). Vertical dashed lines indicate the beginning and end of different seasons (day of year: 83, 139, 220, 284). Shaded areas indicate the standard deviation.

and 2022.

3. Results

3.1. Surface-atmosphere energy exchanges

Differences in mean daily LE across years (2013–2022) between HPC and TVC were small (<10 W m^{-2}) with LE peaking at around 50 ± 30 W m^{-2} (± one standard deviation) at HPC and TVC in July (Fig. 2a). Latent heat flux was low (<10 W m^{-2}) in early spring when air temperature was still below the freezing point. In contrast, mean daily H was around 33 ± 15 W m^{-2} at HPC compared to -5 ± 17 W m^{-2} at TVC in spring (Fig. 2b). The difference in H was smaller in early summer when H peaked at 80 ± 20 W m^{-2} at HPC and at 70 ± 23 W m^{-2} at TVC. Differences in H between the two sites were small (<10 W m^{-2}) in fall. At both sites, H peaked about a month earlier than LE, i.e., in early June versus early July.

Mean daily R_n across years (2013–2022) was generally higher at HPC than at TVC, especially in late winter and spring, reaching a mean daily difference of 61 *W* ± 18 W m^{-2} in spring (Fig. 2c). The lowest difference in R_n was observed during the summer and fall when R_n at HPC was higher by 15 ± 28 W m^{-2} compared to TVC. A further investigation of

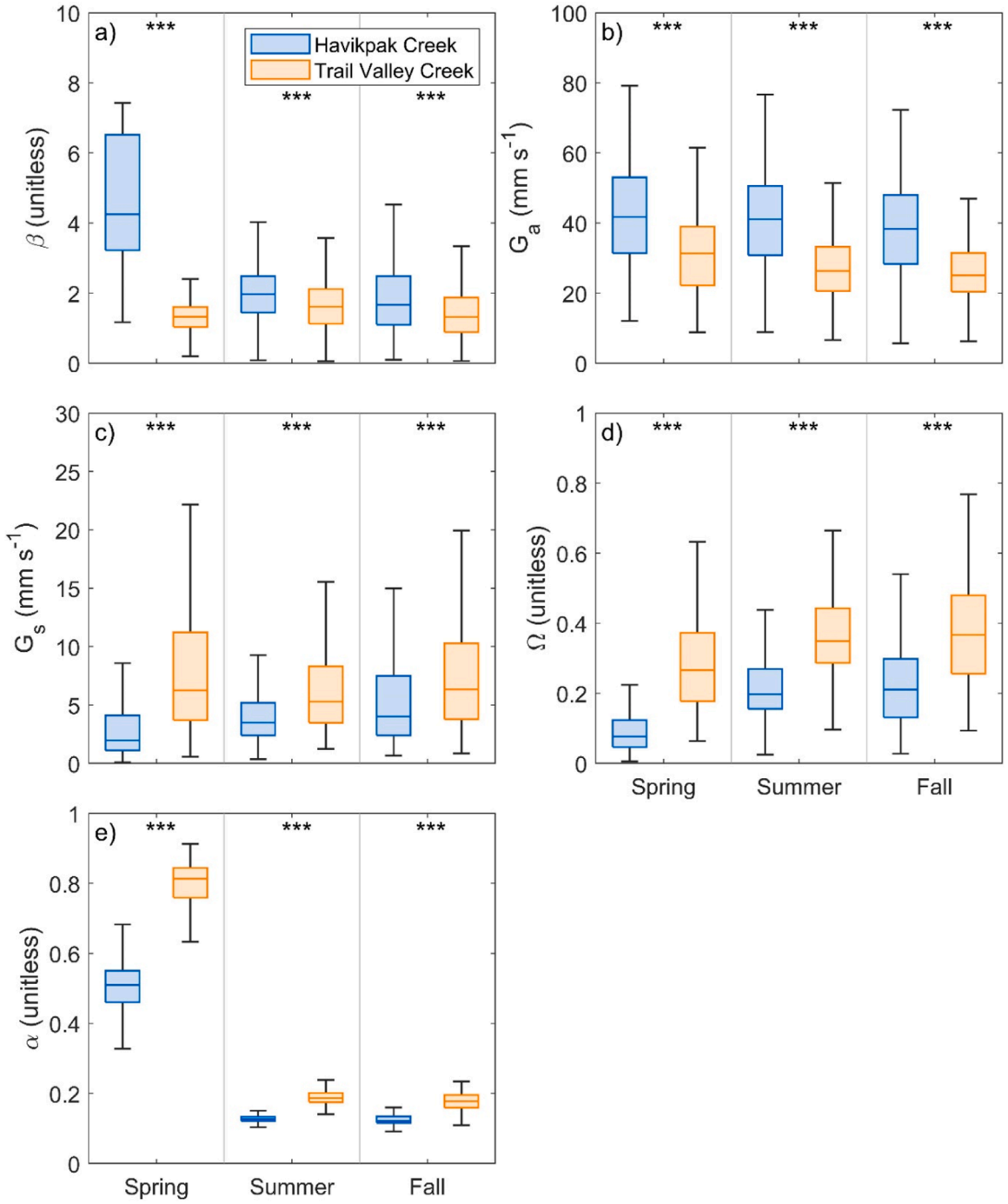

Fig. 3. Differences in seasonal median of daily a) Bowen ratio (β, unitless), b) aerodynamic conductance (G_a, mm s^{-1}), c) surface conductance (G_s, mm s^{-1}), d) decoupling factor (Ω, unitless), and e) albedo (α, unitless) at Havikpak Creek (woodland) and Trail Valley Creek (tundra) between 2013 and 2022. The asterisk (*) indicates the significance-level of the Wilcoxon rank sum test at $\alpha = 0.05$: *p*-value < 0.05 (*), *p*-value < 0.01 (**), and *p*-value < 0.001 (***).

the components of the radiation budget revealed that differences in α were mainly responsible for differences in R_n (Fig. S5). Mean daily G at TVC peaked at 51 ± 24 W m^{-2} in early summer (Fig. 2d) and peaked about a month later at 8.5 ± 2 W m^{-2} at HPC. Ground heat flux was slightly negative (towards atmosphere) during the winter until late spring at both sites and amounted to around 12 ± 6 W m^{-2} in fall at TVC and 3 ± 1 W m^{-2} at HPC.

3.2. Bulk surface properties

The partitioning of available energy at HPC changed rapidly during spring indicated by a steep decrease in β while β slightly increased at TVC from 1.32 to 1.60 (Fig. 3a). The Bowen ratio decreased from spring to fall at HPC while remaining relatively stable at TVC, being around 4.25 and 1.32 in spring and 1.66 and 1.31 in fall at HPC and TVC, respectively. During all seasons, β was significantly lower at TVC than at HPC. As indicated by significantly higher G_a, the efficiency of heat exchange between surface and atmosphere was higher at HPC than at TVC (Fig. 3b). In contrast, G_s was generally higher at TVC than at HPC (Fig. 3c). A significantly higher Ω at TVC indicates that the tundra was less well coupled to the atmosphere than at HPC (Fig. 3d). Daytime median values of Ω were 0.07 and 0.24 in spring, 0.21 and 0.35 in summer, and 0.23 and 0.38 in fall for HPC and TVC, respectively. Both HPC and TVC are more coupled to the atmosphere in spring than in the other seasons. A large difference in α was observed in spring, when TVC reflected about 45% more of incoming shortwave radiation than HPC with a median α of 0.51 at HPC compared to 0.82 at TVC (Fig. 3e). With snowmelt, α decreased rapidly and was similar in summer and fall with around 0.20 for TVC and 0.12 for HPC.

3.3. Atmospheric boundary layer dynamics and characteristics

Mean (2013–2022) tower-based afternoon θ at HPC was generally higher than at TVC throughout the year with the maximum tower-based afternoon θ difference between HPC and TVC reaching 3.5 ± 2.3 °C in spring (Fig. 4a). In spring and summer, tower-based afternoon θ was significantly different, but not in fall (Fig. 4b). In contrast, mean (2013–2022) tower-based afternoon q differences between HPC and TVC were small (<0.1 g kg^{-1}) with a large variability in summer (± 1.1 g kg^{-1}) (Fig. 4c). Afternoon q near the surface was not significantly different across all seasons (Fig. 4d).

A deeper ABL at HPC than at TVC was simulated over the entire year (Fig. 5a). The largest differences between modelled z_i occurred in spring, with a mean (2013–2022) afternoon difference of around 822 ± 138 m. Differences between modelled afternoon z_i at HPC and TVC were smaller in summer and fall with a mean difference of 175 ± 266 m. The ABL

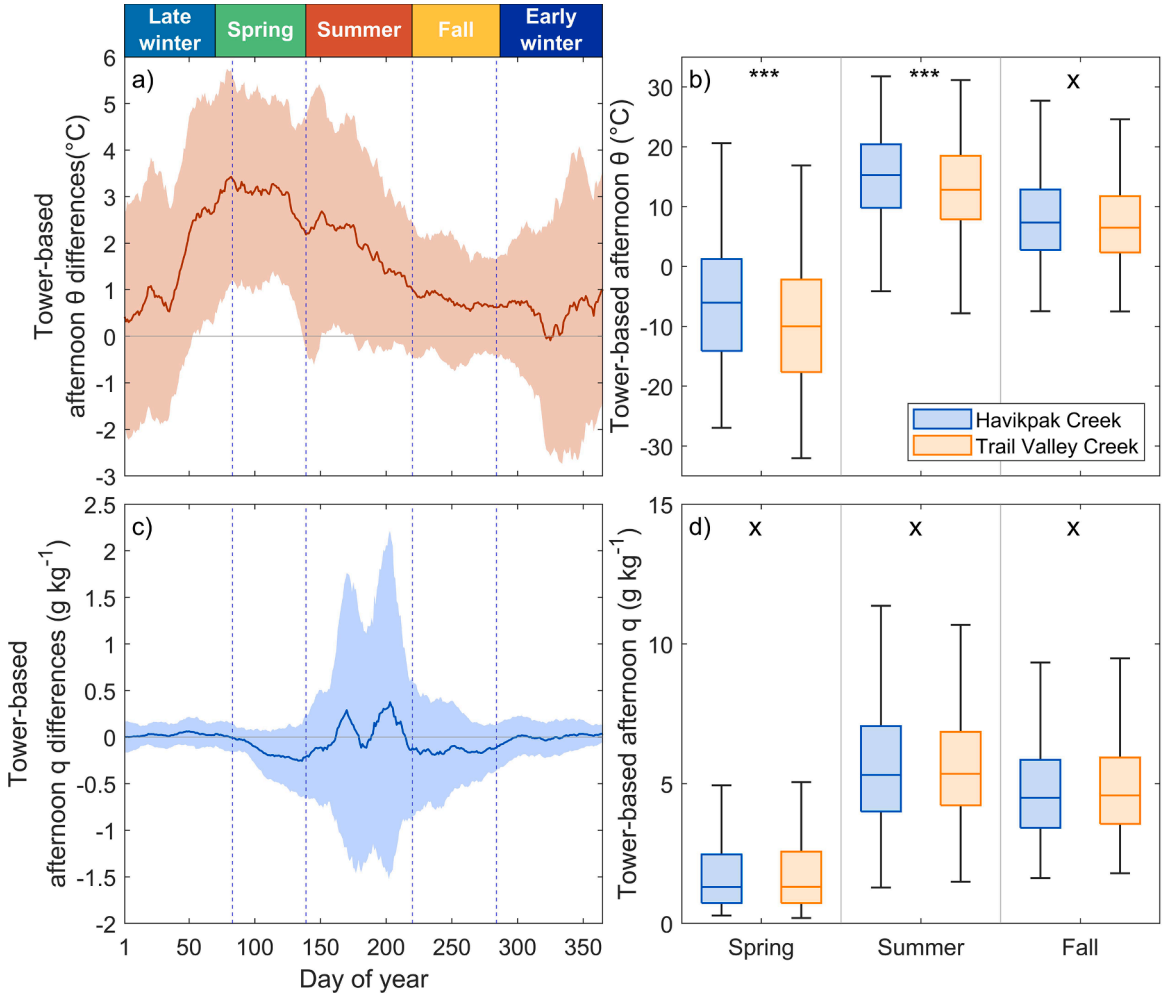

Fig. 4. a) Differences (HPC - TVC) in fourteen-day moving average of mean (± one standard deviation [std]) afternoon tower-based potential temperature (θ,°C) at Havikpak Creek (woodland) and at Trail Valley Creek (tundra) across all years (2013–2022), b) seasonal median of afternoon tower-based θ, c) differences in fourteen-day moving average of mean (± std) afternoon tower-based specific humidity (q, g kg^{-1}) at Havikpak Creek and at Trail Valley Creek across all years (2013–2022), and d) seasonal median of afternoon tower-based q. The asterisk (*) indicates the significance-level of the Wilcoxon rank sum test at $\alpha = 0.05$: p-value < 0.05 (*), p-value < 0.01 (**), and p-value < 0.001 (***).

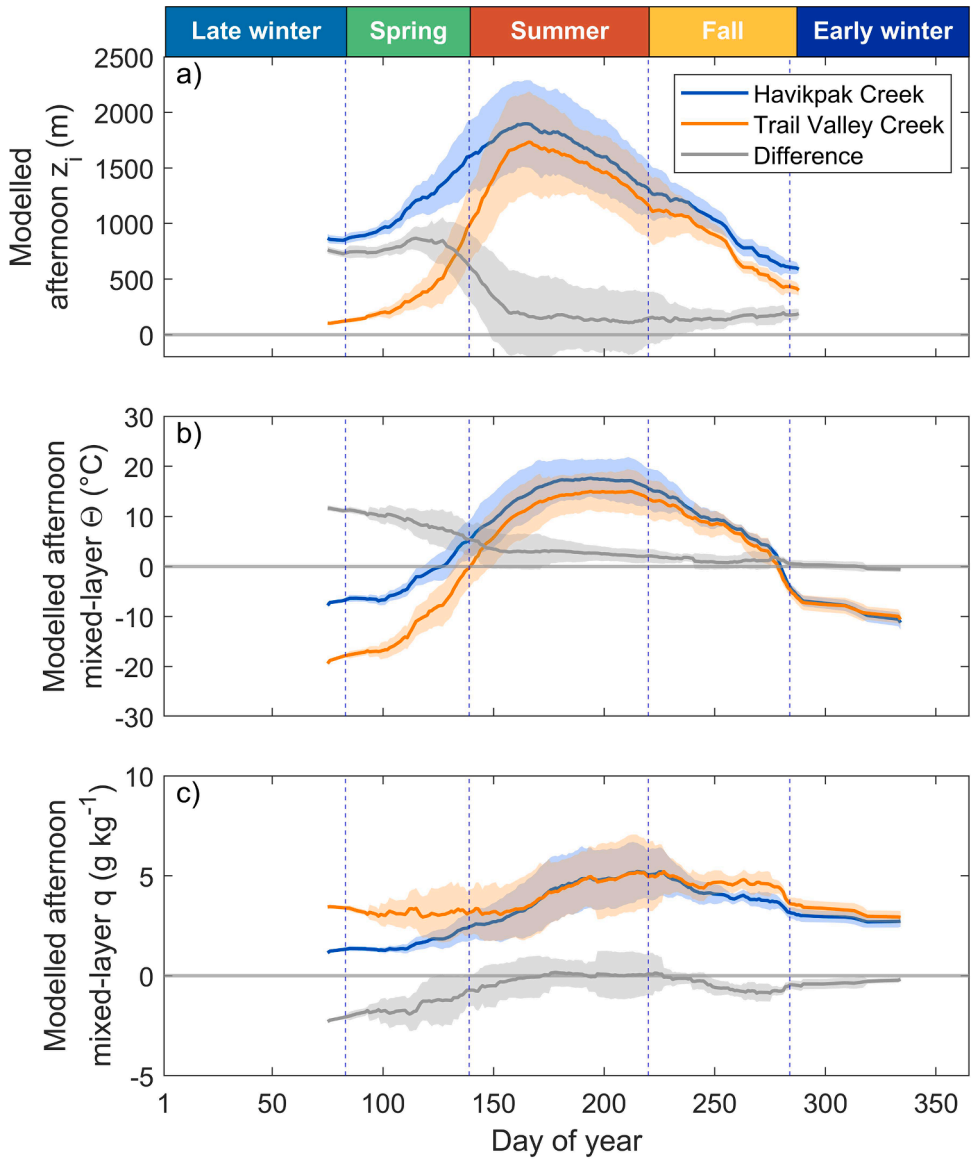

Fig 5. Thirty-day moving averages in modelled (CLASS) a) afternoon atmospheric boundary layer height (z_i, m), b) afternoon mixed-layer potential temperature (θ,° C) and c) afternoon mixed-layer specific humidity (q, g kg^{-1}) at Havikpak Creek (woodland) and Trail Valley Creek (tundra) across all years (2013–2022).

started to substantially grow at TVC only late in spring when H became positive. Differences between modelled afternoon mixed-layer θ followed similar seasonal patterns as differences in modelled afternoon z_i (Fig. 5b). The largest difference occurred in spring with modelled mixed-layer θ being around 9 ± 2.7 °C higher. Differences between modelled mixed-layer θ then gradually decreased to 2.8 ± 2.4 °C on average in summer and 1.4 ± 1.3 °C in fall. Modelled mean afternoon mixed-layer q also showed the largest difference in spring with a mean of 1.7 ± 0.9 g kg^{-1} while differences in summer were below 0.05 ± 0.9 g kg^{-1} and differences in fall were around 0.4 ± 0.3 g kg^{-1} (Fig. 5c).

Diurnal changes in modelled Δθ were significantly different in spring with a median at HPC increasing by around 5.7 °C and at TVC by 2.5 °C over the course of a day (Fig. 6a). In spring, 70% of modelled Δθ at HPC was attributed to surface H while accounting for 88% at TVC, indicating larger entrainment H at HPC. Both surface and entrainment H at HPC in the summer were larger than at TVC leading to an increase of modelled Δθ by 7.6 °C at HPC and by 7 °C at TVC (Fig. 6c, e). In fall, modelled Δθ at HPC and TVC were not significantly different, being respectively 5.6 °C and 5 °C. Surface H at HPC and TVC contributed to modelled Δθ to a similar extent in summer, about two thirds. In fall, 55 % of modelled Δθ at HPC was attributed to surface H while accounting for 65 % at TVC. Overall, surface H at HPC and TVC contributed more to modelled Δθ than entrainment H. A decrease in modelled Δq at HPC by 0.18 g kg^{-1} and an increase in modelled Δq at TVC by 0.2 g kg^{-1} was simulated in spring (Fig. 6b). However, there was large variability in modelled Δq at TVC. Diurnal decrease in q was the largest in summer with 1 g kg^{-1} at HPC and 0.9 g kg^{-1} at TVC, corresponding to the drying from entrainment of dry air (i.e., negative LE) exceeding wetting from surface LE (Fig. 6d, f). There was no significant difference between modelled Δq at HPC and TVC in fall when the drying effect diminished to 0.6 g kg^{-1} and 0.37 g kg^{-1}, respectively.

4. Discussion

4.1. Forest-tundra ecotone in the context of regional climate change

This study showed that surface climate and ABL characteristics varied systematically across two typical sites characteristic of the FTE in the Inuvialuit Settlement Region demonstrating that changes in the FTE distribution can modify regional climate change pathways. However,

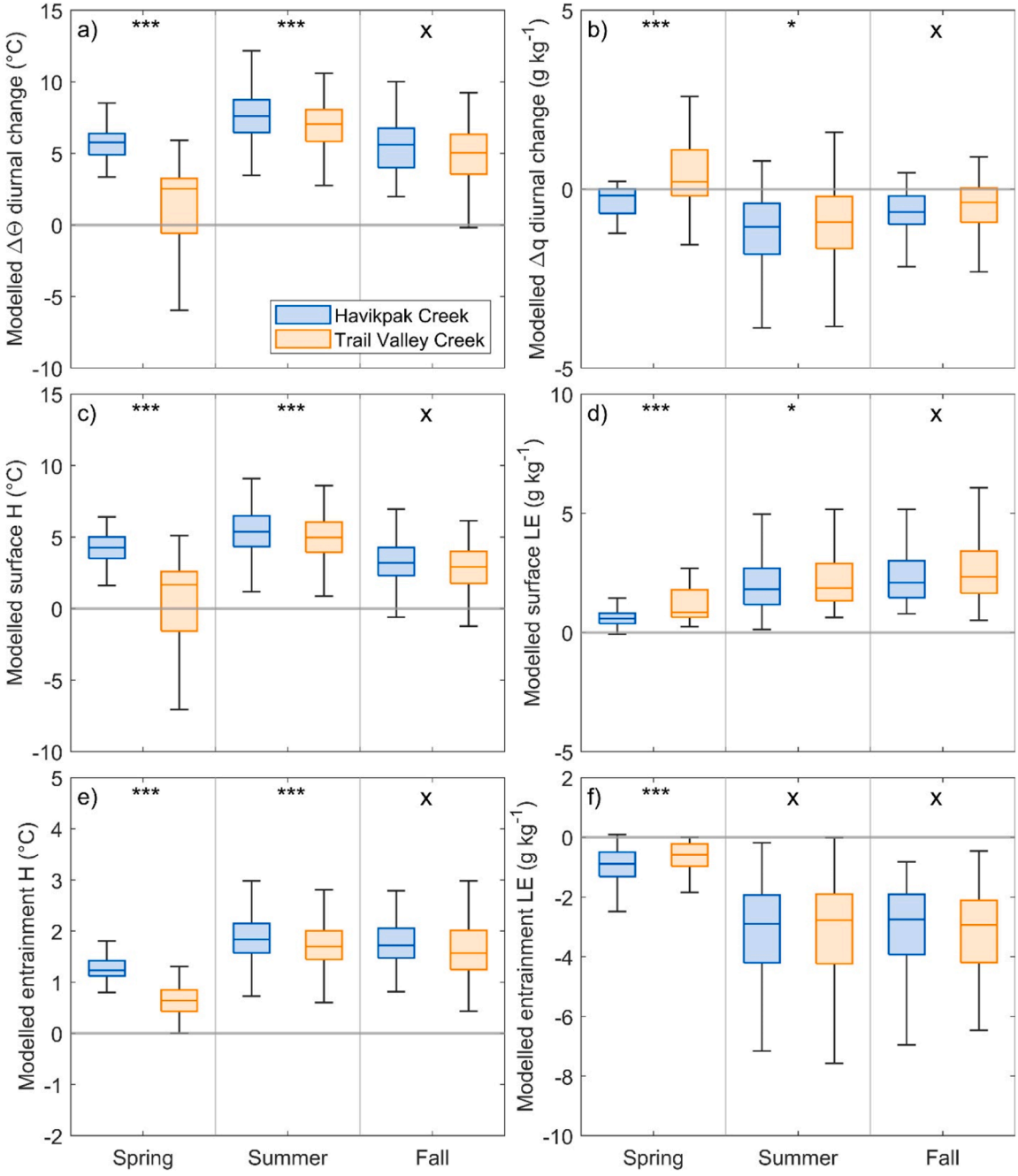

Fig 6. Modelled diurnal changes in a) potential temperature (Δθ,°C), b) specific humidity (Δq, g kg^{-1}) and the contribution from c) surface sensible heat (H, W m^{-2}), d) surface latent heat (LE, W m^{-2}), e) entrainment of H (°C) and f) entrainment of LE (g kg^{-1}) at Havikpak Creek (woodland) and Trail Valley Creek (tundra) across all years (2013–2022). The asterisk (*) indicates the significance-level of the Wilcoxon rank sum test at $\alpha = 0.05$: p-value < 0.05 (*), p-value < 0.01 (**), and p-value < 0.001 (***).

observed and projected FTE changes are complex and highly uncertain. At 52 sites across the FTE in the Northwest Territories, the stand density of white spruce (*Picea glauca* (Moench) Voss) has increased significantly since 1980 (Lantz et al., 2019). Recent tree recruitment has occurred in the FTE but not in the tundra. An increase in alder and spruce stem density from 1970 to 2000 was also found in the Tuktoyaktuk Coastal Plain, NWT, but with no change in their range limits (Travers-Smith and Lantz, 2020). Taller and more productive shrubs were witnessed across the FTE in the Inuvialuit Settlement Region (Lantz et al., 2012). The widespread shrub encroachment affects, for example, snowpack characteristics and distribution (Lantz et al., 2010; Wilcox et al., 2019), and thus the underlying permafrost (Gruber., 2012), and ecosystem services including access to travel routes across the land and traditional livelihoods (Gibson et al., 2021). These changes in vegetation correlate well with the steep increase in air temperature in the region since 1980 (Fig. S1, a, e). While this study was conducted over a tree-dominated woodland and a treeless tundra, current shrub proliferation effects on surface-atmosphere interactions are not well understood in the circumpolar Arctic-boreal region. Our results showed a similar warming effect in the mixed layer from increasing tree cover as reported by Helbig et al. (2016) and Ueyama et al. (2020). Furthermore, modelling results showed that enhanced tree cover leads to a deeper ABL and lower atmospheric moisture in spring and fall but not in summer.

4.2. Surface-atmosphere energy exchanges

In this study, we found H to dominate at HPC with a higher Bowen ratio than at TVC throughout the year, especially in spring. In spring, the trees present at HPC significantly reduce the high reflectivity of the snow-covered ground, resulting in higher available energy compared to TVC. This period of large differences in available energy ends in early June after snow melt. The resulting albedo and radiative differences in spring between tall- and low-stature canopy ecosystems were reported for other northern regions (Baldocchi et al., 2000; Beringer et al., 2005; Lafleur and Rouse, 1995). In summer, albedo differences are smaller. However, darker tree canopies still result in lower albedo and larger available energy.

Evapotranspiration is limited in spring at both study sites. During this period, plant root uptake of water is restricted in frozen soils and physiological chilling and freezing stress additionally reduces stomatal conductance (Baldocchi et al., 2000; Teskey et al., 1984). Latent heat flux remains thus low at HPC and TVC until late spring when LE increases at both sites. During the summer period, HPC and TVC experience similar LE. In our study, the Bowen ratio is higher at HPC than at TVC and remain above 1 year-round at both sites. Similarly, Beringer et al. (2005) found that summer Bowen ratio increased across a gradient from a moist tundra to a moist evergreen forest on the Seward Peninsula in western Alaska. However, they reported lower Bowen ratios across the sites, which could be explained by the fact that the Seward Peninsula is more humid. Another comparative study by Eaton et al. (2001), including our study sites, found higher Bowen ratios at HPC than at TVC, which is consistent with our observations. Similar to Beringer et al. (2005), they reported summertime Bowen ratios at both sites to be lower than in our study (around 0.53 for TVC and 0.98 for HPC). These differences could be explained by the multi-year averages reported here, which likely cover a wider range of environmental conditions than the two-year study by Eaton et al. (2001).

Similar LE and a higher Bowen ratio at HPC compared to TVC indicates that relatively more energy was used to moisten the atmosphere at TVC, while more energy was used to warm the atmosphere at HPC. However, Bowen ratio decreased from spring to fall at HPC, indicating that more energy was used to moisten the atmosphere later in the growing season than early in the growing season. This pattern could partly explain the smaller modelled θ and q differences between HPC and TVC later in the growing season.

4.3. Differences in surface properties across the forest-tundra ecotone

Bulk surface parameters such as G_a and G_s can be useful in providing mechanistic information to diagnose how changes in air temperature and humidity could follow a vegetation shift (Baldocchi and Ma, 2013). For example, rougher surfaces, such as at the woodland site, increase G_a and enhance their ability to transfer mass and energy with the atmosphere (Jarvis and McNaughton 1986; Baldocchi et al., 2000). The higher G_a could contribute to the larger H and deeper ABL in summer over HPC and similar LE despite a lower G_s. Increasing tree coverage then contributes to higher mixed-layer θ and a deeper ABL, with an enhanced ability to transfer heat into the atmosphere (Baldocchi and Ma, 2013).

Similar processes as shown in Beringer et al. (2005) and Thompson et al. (2004) in the Seward Peninsula in western Alaska controlled the energy partitioning in our study region. HPC was more coupled to the atmosphere than TVC, indicating that conditions at the canopy surface were similar to ambient air conditions. Thus, atmospheric conditions such as VPD rather than radiation controlled LE at HPC, which was characterized by a higher VPD. At TVC, R_n was more important in driving LE than at HPC with relatively unrestricted evapotranspiration of moisture from vegetation with low resistance to water loss (Baldocchi et al., 2000; Beringer et al., 2005). In the same way as Beringer et al. (2005), this suggests that tree densification and increases in stem density, as observed the study region (Lantz et al., 2019; Travers-Smith and Lantz, 2020), has the potential to alter the sources and controls of LE, making water loss more sensitive to VPD (Beringer et al., 2005).

4.4. Atmospheric boundary layer dynamics

The ABL height is an important factor controlling regional climate dynamics. Surface fluxes exert a strong control on ABL growth, which affects air temperature and humidity through the entrainment of dry and warm air from the free atmospheres (Baldocchi and Ma, 2013; Denissen et al., 2021; Helbig et al., 2021; Vila-Guerau de Arellano et al., 2015). To fully understand surface-atmosphere interactions across the FTE and to assess how potential vegetation changes could affect the regional climate, changes in the surface energy balance need to be linked to ABL growth feedbacks.

At the FTE in northwestern Canada, the ABL showed important variations in height, θ, and q between the woodland and the tundra site depending on the season. In spring, the large modelled mixed-layer θ difference can be explained by the large difference in H and the quasi-absence of LE to cool the air. Albedo mainly controlled differences in H and played a major role in spring in determining surface climate conditions. However, in summer and fall, albedo differences were smaller and similar LE and small differences in H were found. Modelled mixed-layer θ and q differences were more driven by differences in energy partitioning than in albedo. Differences in modelled mixed-layer θ between HPC and TVC gradually decreased over the year as well as z_i differences, while LE gained in importance and peaked in summer. At TVC, more available energy was used for evapotranspiration, leading to a shallower ABL, cooler and more humid conditions due to the smaller surface H input.

Our results were similar to those of Helbig et al. (2016) and Ueyama et al. (2020) who showed that atmospheric moistening presumably occurred due to a decreased entrainment of dry air by decreased z_i and increased LE. Here, the entrainment of dry air also exceeded the surface input of moisture in summer, leading to a decrease in q over the course of the day in summer and fall. The entrainment of dry air was not significantly different at our sites in summer, resulting in similar moisture in the ABL. Modelled mixed-layer differences in afternoon θ and q followed a pattern similar to the tower observations made near the surface at HPC and TVC (Fig. 4). In both cases, the largest θ differences occurred in spring, and then gradually decreased in summer and fall. However, in spring, differences in observed tower-based θ and q were smaller in magnitude and observed tower-based q differences were less significant than modelled in the mixed layer at HPC and TVC. This highlights the need to consider the influence of ABL growth feedbacks when seeking a comprehensive understanding of regional climate differences.

Similarly, to Ueyama et al. (2020), model simulations resulted in considerable scatter in daily variations of z_i, and mixed-layer $\Delta\theta$ and Δq, but the climatology and magnitude of seasonal variations were well-captured by the model. Contributing to the discrepancies could be the vertical resolution of the radiosonde profiles that varied from 20 m near the surface to 300 m close to z_i. Also, the 'parcel' method strongly depends on surface θ to identify z_i, and the estimated z_i may vary substantially in situations without a pronounced θ inversion at the ABL top (Seibert et al., 2000). For example, when θ slightly increases with height in the mixed layer under slightly stable atmospheric conditions, an underestimation of the z_i can occur. Observations of θ used to evaluate CLASS were made at the Inuvik Upper Air Weather Station (ca. 700 m south-east of HPC), where conditions at the surface are different than at HPC. While surface θ at the two locations were in good agreement, some differences were present and could have influenced the estimation of z_i. Other methods were tested such as the Richardson number method (e.g., Zhang et al., 2014), which resulted in similar results to the 'parcel' method. As also pointed out by Ueyama et al. (2020), estimated initial jumps in θ and q from operational radiosonde observations can

significantly influence the ABL development, and can vary substantially depending on the height at which it was calculated associated with the estimated z_i. While lapse rates in the free atmosphere were similar and supported by observations, assuming similar initial jumps at the entrainment zone in the model could be another cause of error. The causes of the overestimation of z_i in this study remain unclear.

Model simulations showed relatively large discrepancies with observations in spring when surface meteorological conditions differed the most. With large spatial gradients in θ and q, horizontal advection could play an important role in ABL dynamics (Pal et al., 2021). In this study, we did not include horizontal advection terms due to the lack of supporting ground observations. Future studies focusing on mesoscale circulation induced by spatial gradients in θ and q could provide important insights into regional climate dynamics.

The woodland canopy exerted a significant resistance to evapotranspiration and the open nature of the canopy at the FTE caused a disproportionate amount of energy exchange to occur at the soil surface. In boreal forest stands further south, the low rate of evapotranspiration was shown to cause high rates of H and deep ABL enhancing VPD through entrainment of dry air (Baldocchi et al., 2000). Here, we showed that G_a at HPC compensates for lower G_s leading to similar LE at both sites. However, with slightly higher available energy and higher H at HPC and enhanced entrainment of dry air, an increase in tree cover at the FTE could enhance the drought stress on the vegetation and increase wildfire vulnerability (Sedano and Randerson, 2014). Sedano and Randerson (2014) found a significant relationship between VPD and likelihood that a lightning strike would develop into a fire ignition. In the first week after ignition, above average VPD increased the probability that fires would grow to large or very large sizes. Wildfire frequency and intensity is expected to increase at the northern FTE as the climate continues to warm (Chen et al., 2021; Wotton et al., 2017; Young et al., 2017). A change in fire regime at the FTE could shift ecosystems from a carbon sink to a carbon source to the atmosphere and enhance permafrost degradation (Schuur et al., 2008; Walker et al., 2019). Wildfire could also facilitate recruitment of boreal species into areas historically dominated by tundra vegetation (Landhausser and Wein, 1993). These potential changes in z_i, mixed-layer θ and q will also affect regional precipitation patterns, cloud formation and carbon exchanges following vegetation shifts and need further research (Vila-Guerau de Arellano et al., 2015).

5. Conclusion

This study showed the importance of accounting for atmospheric boundary layer growth feedbacks on surface climate to fully understand surface climate differences at the forest-tundra ecotone. A distinct influence of contrasting surface properties across the forest-tundra ecotone on the surface climate was shown along with its seasonal changes. The higher tree cover at the southern margin of the forest-tundra ecotone led to warmer and drier conditions in spring, with albedo, being the main driver of temperature differences. In summer, a higher surface conductance at the tundra site led to relatively more energy being used to moisten the atmosphere, resulting in a shallower atmospheric boundary layer and a regional cooling. The results presented here suggest that tree or shrub densification or encroachment could potentially increase air temperature and cause high rates of sensible heat exchange and deeper atmospheric boundary layer that would enhance the vapour pressure deficit at the forest-tundra ecotone.

This study leveraged routine radiosonde observations made in proximity to the two eddy covariance tower sites. Integrating continuous automated observations of the atmospheric boundary layer to co-located tower-based flux measurements would greatly enhance our ability to predict regional climate changes across the circumpolar Arctic-boreal region and feedbacks on the global climate system following ongoing vegetation shifts.

This study established a baseline understanding of the latitudinal variation in surface-atmosphere interactions and surface climate across the FTE in northwestern Canada. It presents the current state of energy exchange patterns and their impact on surface climate, providing valuable insights for future research in the region. This study contributes to the limited body of research on surface-atmosphere interactions across the FTE and can serve as a valuable reference for future comparisons with other regions and will also help to better understand the impact of potential vegetation change on hydrology, including streamflow and lake levels.

CRediT authorship contribution statement

Vincent Graveline: Methodology, Investigation, Formal analysis, Conceptualization, Software, Visualization, Writing – original draft. **Manuel Helbig:** Conceptualization, Methodology, Supervision, Writing – review & editing. **Gabriel Hould Gosselin:** Data curation, Formal analysis, Resources, Writing – review & editing. **Haley Alcock:** Data curation, Writing – review & editing. **Matteo Detto:** Resources, Writing – review & editing. **Branden Walker:** Writing – review & editing, Resources. **Philip Marsh:** Writing – review & editing, Resources. **Oliver Sonnentag:** Methodology, Funding acquisition, Conceptualization, Project administration, Resources, Supervision, Writing – review & editing.

Declaration of competing interest

The authors declare that they have no known competing financial interests or personal relationships that could have appeared to influence the work reported in this paper.

Data availability

Data will be made available on request.

Acknowledgments

We would like to thank the Inuvialuit community of Inuvik and the Aurora Research Institute granting permission to conduct our research in their homeland. We are grateful for the help of Charles Gauthier and Rosy Tutton who helped during the retrieval of radiosondes in the tundra. Our gratitude also extends to all the people who were present at Trail Valley Creek and made these field campaigns a unique experience. This study was funded through the Canada First Research Excellence Fund's Global Water Futures project Northern Water Futures. V.G. acknowledges funding by Polar Knowledge Canada and Université de Montréal (Programme de mobilité internationale et de courts séjours à l'extérieur du Québec). M.H. acknowledges funding by the Natural Sciences and Engineering Research Council Discovery Grant program. M.D. was supported by the Carbon Mitigation Initiative of Princeton University. P.M. acknowledges funding for research at Trail Valley Creek and Havikpak Creek through the Canada Research Chairs Program (CRC-2019-00335), Natural Sciences and Engineering Council of Canada Discovery Grant and Northern Supplements Program (RGPIN-2022-05347), the Canada Foundation for Innovation "Changing Arctic Network" (CANet, grant no.33661), Natural Resources Canada (Polar Continental Shelf Program, 602-21), Polar Knowledge Canada, and the GNWT Community Impact Monitoring Program (CIMP). O.S. acknowledges funding by the Canada Research Chairs Program (CRC-2018-00259), Canada Foundation for Innovation Leaders Opportunity Fund, Natural Resources Canada (Polar Continental Shelf Program, 608-20), and Natural Sciences and Engineering Research Council Discovery Grant program (DGPIN-2018-05743).

Supplementary materials

Supplementary material associated with this article can be found, in the online version, at doi:10.1016/j.agrformet.2024.109996.

References

Ahmad, S., Bin Lockwood, J.G., 1979. Albedo. Prog. Phys. Geog. 3, 510–543. https://doi.org/10.1177/030913337900300403.

Vila-Guerau de Arellano, J.C., van Heerwaarden, C.J.H., van Stratum, B., van den Dries, K., 2015. Atmospheric Boundary Layer. https://doi.org/10.1017/CBO9781316117422.003.

Baldocchi, D., Ma, S., 2013. How will land use affect air temperature in the surface boundary layer? Lessons learned from a comparative study on the energy balance of an oak savanna and annual grassland in California, USA. Tellus B 65. https://doi.org/10.3402/tellusb.v65i0.19994.

Baldocchi, D., Hincks, B.B., Meyers, T.P., 1988. Measuring biosphere-atmosphere exchanges of biologically related gases with micrometeorological methods. Ecology 69, 1331–1340. https://doi.org/10.2307/1941631.

Baldocchi, D., Kelliher, F.M., Black, T.A., Jarvis, P., 2000. Climate and vegetation controls on boreal zone energy exchange. Glob. Change Biol. 6, 69–83. https://doi.org/10.1046/j.1365-2486.2000.06014.x.

Beck, H.E., Zimmermann, N.E., McVicar, T.R., Vergopolan, N., Berg, A., Wood, E.F., 2018. Present and future Koppen-Geiger climate classification maps at 1-km resolution. Sci. Data 5, 180214. https://doi.org/10.1038/sdata.2018.214.

Beringer, J., Chapin, F.S., Thompson, C.C., McGuire, A.D., 2005. Surface energy exchanges along a tundra-forest transition and feedbacks to climate. Agric. For. Meteorol. 131, 143–161. https://doi.org/10.1016/j.agrformet.2005.05.006.

Berner, L.T., Goetz, S.J., 2022. Satellite observations document trends consistent with a boreal forest biome shift. Glob. Change Biol. https://doi.org/10.1111/gcb.16121.

Bessardon, G.E.Q., Fosu-Amankwah, K., Petersson, A., Brooks, B.J., 2019. Evaluation of Windsond S1H2 performance in Kumasi during the 2016 DACCIWA field campaign. Atmos. Meas. Tech. 12, 1311–1324. https://doi.org/10.5194/amt-12-1311-2019.

Chen, Y., Romps, D.M., Seeley, J.T., Veraverbeke, S., Riley, W.J., Mekonnen, Z.A., Randerson, J.T., 2021. Future increases in Arctic lightning and fire risk for permafrost carbon. Nat. Clim. Change 11, 404–410. https://doi.org/10.1038/s41558-021-01011-y.

Chylek, P., Folland, C., Klett, J.D., Wang, M., Hengartner, N., Lesins, G., Dubey, M.K., 2022. Annual mean arctic amplification 1970–2020: observed and simulated by CMIP6 climate models. Geophys. Res. Lett. 49 https://doi.org/10.1029/2022gl099371.

Davy, R., Esau, I., 2016. Differences in the efficacy of climate forcings explained by variations in atmospheric boundary layer depth. Nat. Commun. 7, 11690. https://doi.org/10.1038/ncomms11690.

Denissen, J.M.C., Orth, R., Wouters, H., Miralles, D.G., van Heerwaarden, C.C., de Arellano, J.V.-G., Teuling, A.J., 2021. Soil moisture signature in global weather balloon soundings. NPJ Clim. Atmos. Sci. 4 https://doi.org/10.1038/s41612-021-00167-w.

Detto, M., Katul, G.G., 2007. Simplified expressions for adjusting higher-order turbulent statistics obtained from open path gas analyzers. Boundary Layer Meteorol. 122, 205–216. https://doi.org/10.1007/s10546-006-9105-1.

Dial, R.J., Maher, C.T., Hewitt, R.E., Wockenfuss, A.M., Wong, R.E., Crawford, D.J., Zietlow, M.G., Sullivan, P.F., 2024. Arctic sea ice retreat fuels boreal forest advance. Science 383 (1979), 877–884. https://doi.org/10.1126/science.adh2339.

Eaton, A.K., Rouse, W.R., Lafleur, P.M., Marsh, P., Blanken, P.D., 2001. Surface energy balance of the western and central Canadian Subarctic: variations in the energy balance among five major Terrain types. J. Clim. 14, 3692–3703. https://doi.org/10.1175/1520-0442(2001)014. <3692:Sebotw>2.0.Co;2.

Foster, A.C., Wang, J.A., Frost, G.V., Davidson, S.J., Hoy, E., Turner, K.W., Sonnentag, O., Epstein, H., Berner, L.T., Armstrong, A.H., Kang, M., Rogers, B.M., Campbell, E., Miner, K.R., Orndahl, K.M., Bourgeau-Chavez, L.L., Lutz, D.A., French, N., Chen, D., Du, J., Shestakova, T.A., Shuman, J.K., Tape, K., Virkkala, A.-M., Potter, C., Goetz, S., 2022. Disturbances in North American boreal forest and Arctic tundra: impacts, interactions, and responses. Environ. Res. Lett. 17 https://doi.org/10.1088/1748-9326/ac98d7.

Gibson, C., Cottenie, K., Gingras-Hill, T., Kokelj, S.V., Baltzer, J.L., Chasmer, L., Turetsky, M.R., 2021. Mapping and understanding the vulnerability of northern peatlands to permafrost thaw at scales relevant to community adaptation planning. Environ. Res. Lett. 16 https://doi.org/10.1088/1748-9326/abe74b.

Goetz, S.J., Bunn, A.G., Fiske, G.J., Houghton, R.A., 2005. Satellite-observed photosynthetic trends across boreal North America associated with climate and fire disturbance. Proc. Natl. Acad. Sci. U.S.A. 102, 13521–13525. https://doi.org/10.1073/pnas.0506179102.

Gonzalez, P., Neilson, R.P., Lenihan, J.M., Drapek, R.J., 2010. Global patterns in the vulnerability of ecosystems to vegetation shifts due to climate change. Glob. Ecol. Biogeogr. 19, 755–768. https://doi.org/10.1111/j.1466-8238.2010.00558.x.

Gruber, S., 2012. Derivation and analysis of a high-resolution estimate of global permafrost zonation. Cryosphere 6, 221–233. https://doi.org/10.5194/tc-6-221-2012.

Hansen, M.C., Potapov, P.V., Moore, R., Hancher, M., Turubanova, S.A., Tyukavina, A., Thau, D., Stehman, S.V., Goetz, S.J., Loveland, T.R., Kommareddy, A., Egorov, A., Chini, L., Justice, C.O., Townshend, J.R.G., 2013. High-resolution global maps of 21st-century forest cover change. Science 342 (1979), 850–853. https://doi.org/10.1126/science.1244693.

Harsch, M.A., Hulme, P.E., McGlone, M.S., Duncan, R.P., 2009. Are treelines advancing? A global meta-analysis of treeline response to climate warming. Ecol. Lett. 12, 1040–1049. https://doi.org/10.1111/j.1461-0248.2009.01355.x.

Helbig, M., Pappas, C., Sonnentag, O., 2016. Permafrost thaw and wildfire: equally important drivers of boreal tree cover changes in the Taiga Plains, Canada. Geophys. Res. Lett. 43, 1598–1606. https://doi.org/10.1002/2015gl067193.

Helbig, M., Wischnewski, K., Kljun, N., Chasmer, L.E., Quinton, W.L., Detto, M., Sonnentag, O., 2016. Regional atmospheric cooling and wetting effect of permafrost thaw-induced boreal forest loss. Glob. Change Biol. 22, 4048–4066. https://doi.org/10.1111/gcb.13348.

Helbig, M., Chasmer, L.E., Desai, A.R., Kljun, N., Quinton, W.L., Sonnentag, O., 2017. Direct and indirect climate change effects on carbon dioxide fluxes in a thawing boreal forest-wetland landscape. Glob. Change Biol. 23, 3231–3248. https://doi.org/10.1111/gcb.13638.

Helbig, M., Waddington, J.M., Alekseychik, P., Amiro, B.D., Aurela, M., Barr, A.G., Black, T.A., Carey, S.K., Chen, J., Chi, J., Desai, A.R., Dunn, A., Euskirchen, E.S., Flanagan, L.B., Friborg, T., Garneau, M., Grelle, A., Harder, S., Heliasz, M., Humphreys, E.R., Ikawa, H., Isabelle, P.-E., Iwata, H., Jassal, R., Korkiakoski, M., Kurbatova, J., Kutzbach, L., Lapshina, E., Lindroth, A.M., Löfvenius, M.O., Lohila, A., Mammarella, I., Marsh, P., Moore, P.A., Maximov, T., Nadeau, D.F., Nicholls, E.M., Nilsson, M.B., Ohta, T., Peichl, M., Petrone, R.M., Prokushkin, A., Quinton, W.L., Roulet, N., Runkle, B.R.K., Sonnentag, O., Strachan, I.B., Taillardat, P., Tuittila, E.-S., Tuovinen, J.-P., Turner, J., Ueyama, M., Varlagin, A., Vesala, T., Wilmking, M., Zyrianov, V., 2020. The biophysical climate mitigation potential of boreal peatlands during the growing season. Environ. Res. Lett. https://doi.org/10.1088/1748-9326/abab34.

Helbig, M., Gerken, T., Beamesderfer, E.R., Baldocchi, D.D., Banerjee, T., Biraud, S.C., Brown, W.O.J., Brunsell, N.A., Burakowski, E.A., Burns, S.P., Butterworth, B.J., Chan, W.S., Davis, K.J., Desai, A.R., Fuentes, J.D., Hollinger, D.Y., Kljun, N., Mauder, M., Novick, K.A., Perkins, J.M., Rahn, D.A., Rey-Sanchez, C., Santanello, J. A., Scott, R.L., Seyednasrollah, B., Stoy, P.C., Sullivan, R.C., de Arellano, J.V.-G., Wharton, S., Yi, C., Richardson, A.D., 2021. Integrating continuous atmospheric boundary layer and tower-based flux measurements to advance understanding of land-atmosphere interactions. Agric. For. Meteorol. 307 https://doi.org/10.1016/j.agrformet.2021.108509.

Hersbach, H., Bell, B., Berrisford, P., Biavati, G., Horányi, A., Muñoz Sabater, J., Nicolas, J., Peubey, C., Radu, R., Rozum, I., Schepers, D., Simmons, A., Soci, C., Dee, D., Thépaut, J.-N., 2023. ERA5 Hourly Data on Pressure Levels from 1940 to Present. https://doi.org/10.24381/cds.bd0915c6.

Holzworth, G.C., 1964. Estimates of mean maximum mixing depths in the contiguous United States. Mon. Weather. Rev. 92, 235–242. https://doi.org/10.1175/1520-0493 (1964)092<0235:Eommmd>2.3.Co;2.

Hopkinson, R.F., McKenney, D.W., Milewska, E.J., Hutchinson, M.F., Papadopol, P., Vincent, L.A., 2011. Impact of aligning climatological day on gridding daily maximum–minimum temperature and precipitation over Canada. J. Appl. Meteorol. Climatol. 50, 1654–1665. https://doi.org/10.1175/2011jamc2684.1.

Jarvis, P.G., McNaughton, K.G., 1986. Stomatal control of transpiration: scaling up from leaf to region. In: MacFadyen, A., Ford, E.D. (Eds.), Advances in Ecological Research. Academic Press, pp. 1–49. https://doi.org/10.1016/S0065-2504(08)60119-1.

Knauer, J., El-Madany, T.S., Zaehle, S., Migliavacca, M., 2018. Bigleaf-an R package for the calculation of physical and physiological ecosystem properties from eddy covariance data. PLoS ONE 13, e0201114. https://doi.org/10.1371/journal.pone.0201114.

Krogh, S.A., Pomeroy, J.W., 2018. Recent changes to the hydrological cycle of an Arctic basin at the tundra–taiga transition. Hydrol Earth Syst Sci 22, 3993–4014. https://doi.org/10.5194/hess-22-3993-2018.

Lafleur, P.M., Rouse, W.R., 1995. Energy partitioning at treeline forest and tundra sites and its sensitivity to climate change. Atmosphere 33, 121–133. https://doi.org/10.1080/07055900.1995.9649527.

Landhausser, S.M., Wein, R.W., 1993. Postfire vegetation recovery and tree establishment at the arctic treeline: climate-change-vegetation-response hypotheses. J. Ecol. 81 https://doi.org/10.2307/2261664.

Lantz, T.C., Gergel, S.E., Kokelj, S.V., 2010. Spatial heterogeneity in the shrub tundra ecotone in the Mackenzie Delta Region, Northwest Territories: implications for arctic environmental change. Ecosystems 13, 194–204. https://doi.org/10.1007/s10021-009-9310-0.

Lantz, T.C., Marsh, P., Kokelj, S.V., 2012. Recent shrub proliferation in the mackenzie delta uplands and microclimatic implications. Ecosystems 16, 47–59. https://doi.org/10.1007/s10021-012-9595-2.

Lantz, T.C., Moffat, N.D., Fraser, R.H., Walker, X., 2019. Reproductive limitation mediates the response of white spruce (Picea glauca) to climate warming across the forest–tundra ecotone. Arct. Sci. 5, 167–184. https://doi.org/10.1139/as-2018-0012.

Lewis, J.M., 1995. The story behind the Bowen ratio. Bull. Am. Meteorol. Soc. 76, 2433–2443.

Marsh, P., Pomeroy, J.W., 1996. Meltwater Fluxes at an Arctic Forest-Tundra Site. Hydrol Process 10, 1383–1400. doi:10.1002/(sici)1099-1085(199610)10:10<1383::Aid-hyp468>3.0.Co;2-w.

Mauder, M., Foken, T., 2011. Documentation and Instruction Manual of the Eddy-Covariance Software Package TK3.

McGuire, A.D., Chapin, F.S., Walsh, J.E., Wirth, C., 2006. Integrated regional changes in arctic climate feedbacks: implications for the global climate system. Annu Rev. Environ. Resour. 31, 61–91. https://doi.org/10.1146/annurev.energy.31.020105.100253.

McKenney, D.W., Hutchinson, M.F., Papadopol, P., Lawrence, K., Pedlar, J., Campbell, K., Milewska, E., Hopkinson, R.F., Price, D., Owen, T., 2011. Customized

spatial climate models for North America. Bull. Am. Meteorol. Soc. 92, 1611–1622. https://doi.org/10.1175/2011bams3132.1.
Moncrieff, J.B., Massheder, J.M., de Bruin, H., Elbers, J., Friborg, T., Heusinkveld, B., Kabat, P., Scott, S., Soegaard, H., Verhoef, A., 1997. A system to measure surface fluxes of momentum, sensible heat, water vapour and carbon dioxide. J. Hydrol. 188–189, 589–611. https://doi.org/10.1016/s0022-1694(96)03194-0.
Monteith, J.L., 1965. Evaporation and environment. Symp. Soc. Exp. Biol. 19, 205–234.
Montesano, P.M., Neigh, C.S.R., Macander, M., Feng, M., Noojipady, P., 2020. The bioclimatic extent and pattern of the cold edge of the boreal forest: the circumpolar taiga-tundra ecotone. Environ. Res. Lett. 15 https://doi.org/10.1088/1748-9326/abb2c7.
Myers-Smith, I.H., Forbes, B.C., Wilmking, M., Hallinger, M., Lantz, T., Blok, D., Tape, K. D., Macias-Fauria, M., Sass-Klaassen, U., Lévesque, E., Boudreau, S., Ropars, P., Hermanutz, L., Trant, A., Collier, L.S., Weijers, S., Rozema, J., Rayback, S.A., Schmidt, N.M., Schaepman-Strub, G., Wipf, S., Rixen, C., Ménard, C.B., Venn, S., Goetz, S., Andreu-Hayles, L., Elmendorf, S., Ravolainen, V., Welker, J., Grogan, P., Epstein, H.E., Hik, D.S., 2011. Shrub expansion in tundra ecosystems: dynamics, impacts and research priorities. Environ. Res. Lett. 6 https://doi.org/10.1088/1748-9326/6/4/045509.
Oechel, W.C., Laskowski, C.A., Burba, G., Gioli, B., Kalhori, A.A.M., 2014. Annual patterns and budget of CO2 flux in an Arctic tussock tundra ecosystem. J. Geophys. Res. Biogeosci. 119, 323–339. https://doi.org/10.1002/2013jg002431.
Pal, S., Clark, N.E., Lee, T.R., Conder, M., Buban, M., 2021. When and where horizontal advection is critical to alter atmospheric boundary layer dynamics over land: the need for a conceptual framework. Atmos. Res. 264 https://doi.org/10.1016/j.atmosres.2021.105825.
Papale, D., Reichstein, M., Aubinet, M., Canfora, E., Bernhofer, C., Kutsch, W., Longdoz, B., Rambal, S., Valentini, R., Vesala, T., Yakir, D., 2006. Towards a standardized processing of Net Ecosystem Exchange measured with eddy covariance technique: algorithms and uncertainty estimation. Biogeosciences. 3, 571–583. https://doi.org/10.5194/bg-3-571-2006.
Pearson, R.G., Phillips, S.J., Loranty, M.M., Beck, P.S.A., Damoulas, T., Knight, S.J., Goetz, S.J., 2013. Shifts in Arctic vegetation and associated feedbacks under climate change. Nat. Clim. Change 3, 673–677. https://doi.org/10.1038/nclimate1858.
Phoenix, G.K., Bjerke, J.W., 2016. Arctic browning: extreme events and trends reversing arctic greening. Glob. Change Biol. 22, 2960–2962. https://doi.org/10.1111/gcb.13261.
Qu, B., Roy, A., Melton, J.R., Black, T.A., Amiro, B., Euskirchen, E.S., Ueyama, M., Kobayashi, H., Schulze, C., Gosselin, G.H., Cannon, A.J., Detto, M., Sonnentag, O., 2023. A boreal forest model benchmarking dataset for North America: a case study with the Canadian Land Surface Scheme Including Biogeochemical Cycles (CLASSIC). Environ. Res. Lett. 18 https://doi.org/10.1088/1748-9326/ace376.
R Core Team, 2020. R: A Language and Environment for Statistical Computing.
Rantanen, M., Karpechko, A.Y., Lipponen, A., Nordling, K., Hyvärinen, O., Ruosteenoja, K., Vihma, T., Laaksonen, A., 2022. The Arctic has warmed nearly four times faster than the globe since 1979. Commun. Earth. Environ. 3 https://doi.org/10.1038/s43247-022-00498-3.
Reichstein, M., Falge, E., Baldocchi, D., Papale, D., Aubinet, M., Berbigier, P., Bernhofer, C., Buchmann, N., Gilmanov, T., Granier, A., Grunwald, T., Havrankova, K., Ilvesniemi, H., Janous, D., Knohl, A., Laurila, T., Lohila, A., Loustau, D., Matteucci, G., Meyers, T., Miglietta, F., Ourcival, J.-M., Pumpanen, J., Rambal, S., Rotenberg, E., Sanz, M., Tenhunen, J., Seufert, G., Vaccari, F., Vesala, T., Yakir, D., Valentini, R., 2005. On the separation of net ecosystem exchange into assimilation and ecosystem respiration: review and improved algorithm. Glob. Change Biol. 11, 1424–1439. https://doi.org/10.1111/j.1365-2486.2005.001002.x.
Rowlandson, T.L., Berg, A.A., Bullock, P.R., Ojo, E.R., McNairn, H., Wiseman, G., Cosh, M.H., 2013. Evaluation of several calibration procedures for a portable soil moisture sensor. J. Hydrol. 498, 335–344. https://doi.org/10.1016/j.jhydrol.2013.05.021.
Ryu, Y., Baldocchi, D.D., Ma, S., Hehn, T., 2008. Interannual variability of evapotranspiration and energy exchange over an annual grassland in California. J. Geophys. Res. 113 https://doi.org/10.1029/2007jd009263.
Ryu, Y., Nilson, T., Kobayashi, H., Sonnentag, O., Law, B.E., Baldocchi, D.D., 2010. On the correct estimation of effective leaf area index: does it reveal information on clumping effects? Agric. For. Meteorol. 150, 463–472. https://doi.org/10.1016/j.agrformet.2010.01.009.
Scheffer, M., Hirota, M., Holmgren, M., Van Nes, E.H., Chapin 3rd, F.S., 2012. Thresholds for boreal biome transitions. Proc. Natl. Acad. Sci. U. S. A. 109, 21384–21389. https://doi.org/10.1073/pnas.1219844110.
Schuur, E.A.G., Bockheim, J., Canadell, J.G., Euskirchen, E., Field, C.B., Goryachkin, S. V., Hagemann, S., Kuhry, P., Lafleur, P.M., Lee, H., Mazhitova, G., Nelson, F.E., Rinke, A., Romanovsky, V.E., Shiklomanov, N., Tarnocai, C., Venevsky, S., Vogel, J. G., Zimov, S.A., 2008. Vulnerability of permafrost carbon to climate change: implications for the global carbon cycle. Bioscience 58, 701–714. https://doi.org/10.1641/b580807.
Sedano, F., Randerson, J.T., 2014. Multi-scale influence of vapor pressure deficit on fire ignition and spread in boreal forest ecosystems. Biogeosciences. 11, 3739–3755. https://doi.org/10.5194/bg-11-3739-2014.
Seibert, P., 2000. Review and intercomparison of operational methods for the determination of the mixing height. Atmos. Environ. 34, 1001–1027. https://doi.org/10.1016/s1352-2310(99)00349-0.
Seidel, D.J., Ao, C.O., Li, K., 2010. Estimating climatological planetary boundary layer heights from radiosonde observations: comparison of methods and uncertainty analysis. J. Geophys. Res. 115 https://doi.org/10.1029/2009jd013680.
Sonnentag, O., Chen, J.M., Roberts, D.A., Talbot, J., Halligan, K.Q., Govind, A., 2007a. Mapping tree and shrub leaf area indices in an ombrotrophic peatland through multiple endmember spectral unmixing. Remote Sens. Environ. 109, 342–360. https://doi.org/10.1016/j.rse.2007.01.010.
Sonnentag, O., Talbot, J., Chen, J.M., Roulet, N.T., 2007b. Using direct and indirect measurements of leaf area index to characterize the shrub canopy in an ombrotrophic peatland. Agric. For. Meteorol. 144, 200–212. https://doi.org/10.1016/j.agrformet.2007.03.001.
Stoy, P.C., Mauder, M., Foken, T., Marcolla, B., Boegh, E., Ibrom, A., Arain, M.A., Arneth, A., Aurela, M., Bernhofer, C., Cescatti, A., Dellwik, E., Duce, P., Gianelle, D., van Gorsel, E., Kiely, G., Knohl, A., Margolis, H., McCaughey, H., Merbold, L., Montagnani, L., Papale, D., Reichstein, M., Saunders, M., Serrano-Ortiz, P., Sottocornola, M., Spano, D., Vaccari, F., Varlagin, A., 2013. A data-driven analysis of energy balance closure across FLUXNET research sites: the role of landscape scale heterogeneity. Agric. For. Meteorol. 171–172, 137–152. https://doi.org/10.1016/j.agrformet.2012.11.004.
Stull, R., 1988. The atmospheric boundary layer. In: Library, A.S. (Ed.), An Introduction to Boundary Layer Meteorology. Springer, Dordrecht. https://doi.org/10.1007/978-94-009-3027-8.
Tape, K.E.N., Sturm, M., Racine, C., 2006. The evidence for shrub expansion in Northern Alaska and the Pan-Arctic. Glob. Change Biol. 12, 686–702. https://doi.org/10.1111/j.1365-2486.2006.01128.x.
Tennekes, H., Driedonks, A.G.M., 1981. Basic entrainment equations for the atmospheric boundary layer. Boundary Layer Meteorol. 20, 515–531. https://doi.org/10.1007/bf00122299.
Tennekes, H., 1973. A model for the dynamics of the inversion above a convective boundary layer. J. Atmos. Sci. 30, 558–567. https://doi.org/10.1175/1520-0469(1973)030<0558:Amftdo>2.0.Co;2.
Teskey, R.O., Hinckley, T.M., Grier, C.C., 1984. Temperature-induced change in the water relations of Abies amabilis (Dougl.) forbes. Plant Physiol. 74, 77–80.
Thom, A.S., 1972. Momentum, mass and heat exchange of vegetation. Quart. J. R. Meteorol. Soc. 98, 124–134. https://doi.org/10.1002/qj.49709841510.
Thompson, C., Beringer, J., Chapin, F.S., McGuire, A.D., 2004. Structural complexity and land-surface energy exchange along a gradient from arctic tundra to boreal forest. J. Veg. Sci. 15, 397–406. https://doi.org/10.1111/j.1654-1103.2004.tb02277.x.
Timoney, K.P., Mamet, S., 2020. No treeline advance over the last 50 years in subarctic western and central Canada and the problem of vegetation misclassification in remotely sensed data. Écoscience 27, 93–106. https://doi.org/10.1080/11956860.2019.1698258.
Timoney La Roi, G.H., Zoltai, S.C., Robinson, A.L., 1992. The high subarctic Forest-Tundra of Northwestern Canada: position, width, and vegetation gradients in relation to climate. Arctic 45. https://doi.org/10.14430/arctic1367.
Travers-Smith, H.Z., Lantz, T.C., 2020. Leading-edge disequilibrium in alder and spruce populations across the forest–tundra ecotone. Ecosphere 11. https://doi.org/10.1002/ecs2.3118.
Trenberth, K.E., 2011. Changes in precipitation with climate change. Clim. Res. 47, 123–138. https://doi.org/10.3354/cr00953.
Ueyama, M., Yamamori, T., Iwata, H., Harazono, Y., 2020. Cooling and moistening of the planetary boundary layer in interior alaska due to a postfire change in surface energy exchange. J. Geophys. Res. 125 https://doi.org/10.1029/2020jd032968.
Van Dijk, A.I.J.M., Dolman, A.J., 2004. Estimates of CO2 uptake and release among European forests based on eddy covariance data. Glob. Change Biol. 10, 1445–1459. https://doi.org/10.1111/j.1365-2486.2004.00831.x.
van Heerwaarden, C.C., Teuling, A.J., 2014. Disentangling the response of forest and grassland energy exchange to heatwaves under idealized land–atmosphere coupling. Biogeosciences. 11, 6159–6171. https://doi.org/10.5194/bg-11-6159-2014.
Vickers, D., Mahrt, L., 1997. Quality control and flux sampling problems for tower and aircraft data. J. Atmos. Ocean. Technol. 14, 512–526. https://doi.org/10.1175/1520-0426(1997)014<0512:Qcafsp>2.0.Co;2.
Walker, X.J., Baltzer, J.L., Cumming, S.G., Day, N.J., Ebert, C., Goetz, S., Johnstone, J.F., Potter, S., Rogers, B.M., Schuur, E.A.G., Turetsky, M.R., Mack, M.C., 2019. Increasing wildfires threaten historic carbon sink of boreal forest soils. Nature 572, 520–523. https://doi.org/10.1038/s41586-019-1474-y.
Wallace, C.A., Baltzer, J.L., 2019. Tall shrubs mediate abiotic conditions and plant communities at the taiga–tundra ecotone. Ecosystems. 23, 828–841. https://doi.org/10.1007/s10021-019-00435-0.
Wang, J.A., Sulla-Menashe, D., Woodcock, C.E., Sonnentag, O., Keeling, R.F., Friedl, M. A., 2020. Extensive land cover change across Arctic-Boreal Northwestern North America from disturbance and climate forcing. Glob. Change Biol. 26, 807–822. https://doi.org/10.1111/gcb.14804.
Webb, E.K., Pearman, G.I., Leuning, R., 1980. Correction of flux measurements for density effects due to heat and water vapour transfer. Quart. J. R. Meteorol. Soc. 106, 85–100. https://doi.org/10.1002/qj.49710644707.
Wilcox, E.J., Keim, D., de Jong, T., Walker, B., Sonnentag, O., Sniderhan, A.E., Mann, P., Marsh, P., 2019. Tundra shrub expansion may amplify permafrost thaw by advancing snowmelt timing. Arct. Sci. 5, 202–217. https://doi.org/10.1139/as-2018-0028.
Wilczak, J.M., Oncley, S.P., Stage, S.A., 2001. Sonic anemometer tilt correction algorithms. Boundary Layer Meteorol. 99, 127–150. https://doi.org/10.1023/a:1018966204465.
Wilson, K., Goldstein, A., Falge, E., Aubinet, M., Baldocchi, D., Berbigier, P., Bernhofer, C., Ceulemans, R., Dolman, H., Field, C., Grelle, A., Ibrom, A., Law, B.E., Kowalski, A., Meyers, T., Moncrieff, J., Monson, R., Oechel, W., Tenhunen, J., Valentini, R., Verma, S., 2002. Energy balance closure at FLUXNET sites. Agric. For. Meteorol. 113, 223–243. https://doi.org/10.1016/s0168-1923(02)00109-0.
Wisser, D., Marchenko, S., Talbot, J., Treat, C., Frolking, S., 2011. Soil temperature response to 21st century global warming: the role of and some implications for peat

carbon in thawing permafrost soils in North America. Earth Syst. Dynam. 2, 121–138. https://doi.org/10.5194/esd-2-121-2011.

Wotton, B.M., Flannigan, M.D., Marshall, G.A., 2017. Potential climate change impacts on fire intensity and key wildfire suppression thresholds in Canada. Environ. Res. Lett. 12 https://doi.org/10.1088/1748-9326/aa7e6e.

Xu, T., Hutchinson, M.F., 2013. New developments and applications in the ANUCLIM spatial climatic and bioclimatic modelling package. Environ. Model. Softw. 40, 267–279. https://doi.org/10.1016/j.envsoft.2012.10.003.

Young, A.M., Higuera, P.E., Duffy, P.A., Hu, F.S., 2017. Climatic thresholds shape northern high-latitude fire regimes and imply vulnerability to future climate change. Ecography. 40, 606–617. https://doi.org/10.1111/ecog.02205.

Zhang, W., Miller, P.A., Smith, B., Wania, R., Koenigk, T., Döscher, R., 2013. Tundra shrubification and tree-line advance amplify arctic climate warming: results from an individual-based dynamic vegetation model. Environ. Res. Lett. 8 https://doi.org/10.1088/1748-9326/8/3/034023.

Zhang, Y., Gao, Z., Li, D., Li, Y., Zhang, N., Zhao, X., Chen, J., 2014. On the computation of planetary boundary-layer height using the bulk Richardson number method. Geosci. Model. Dev. 7, 2599–2611. https://doi.org/10.5194/gmd-7-2599-2014.

Zhu, Z., Piao, S., Lian, X., Myneni, R.B., Peng, S., Yang, H., 2017. Attribution of seasonal leaf area index trends in the northern latitudes with “optimally” integrated ecosystem models. Glob. Change Biol. 23, 4798–4813. https://doi.org/10.1111/gcb.13723.